International Journal of Mining Science and Technology 32 (2022) 487–497

Contents lists available at ScienceDirect

International Journal of Mining Science and Technology

journal homepage: www.elsevier.com/locate/ijmst

Acoustic emission source location method and experimental verification for structures containing unknown empty areas

Longjun Dong [a], Qing Tao [a], Qingchun Hu [a,*], Sijia Deng [a], Yongchao Chen [a], Qiaomu Luo [a], Xihong Zhang [b]

[a] School of Resources and Safety Engineering, Central South University, Changsha 410083, China
[b] School of Civil and Mechanical Engineering, Curtin University, Perth 6102, Australia

ARTICLE INFO

Article history:
Received 1 July 2021
Received in revised form 17 November 2021
Accepted 10 January 2022
Available online 31 January 2022

Keywords:
Acoustic emission
Source location
Empty area identification

ABSTRACT

Acoustic emission (AE) localization plays an important role in the prediction and control of potential hazardous sources in complex structures. However, existing location methods have less discussion on the presence of unknown empty areas. This paper proposes an AE source location method for structures containing unknown empty areas (SUEA). Firstly, this method identifies the shape, size, and location of empty areas in the unknown region by exciting the active AE sources and using the collected AE arrivals. Then, the unknown AE source can be located considering the identified empty areas. The lead break experiments were performed to verify the effectiveness and accuracy of the proposed method. Five specimens were selected containing empty areas with different positions, shapes, and sizes. Results show the average location accuracy of the SUEA increased by 78% compared to the results of the existing method. It can provide a more accurate solution for locating AE sources in complex structures containing unknown empty areas such as tunnels, bridges, railroads, and caves in practical engineering.

1. Introduction

As a passive non-destructive testing (NDT) technique, acoustic emission (AE) technology has a wide range of applications in aerospace [1], engineering machinery [2], mining [3], tunnels [4], bridges [5], railroads [6], and other fields [7–9]. It uses AE signals generated by the material itself during plastic deformation, crack expansion, and impact to perform damage identification, defect recognition, and crack tracing. The main goal of AE monitoring techniques is to determine the location of the AE source. The localization accuracy reflects the degree of conformity between the detected sources and the actual sources [10,11]. The abnormal areas widely existing in engineering structures, such as tunnels, underground mined-out area, water, faults, and other irregular holes, have a significant influence on localization accuracy. It is very difficult to prevent and control the engineering disasters, including sudden water, mud gushing, roofing, rockburst, and structure failure under the conditions with inaccurate locations of AE sources [12,13]. Therefore, it is urgent and important to locate AE sources accurately after detecting and sizing empty areas for reducing and controlling hazard risks in practical engineering.

In recent years, some works have been carried out to improve localization accuracy considering the different conditions, including modal and frequency analysis [14], laser time reversal [15], linear layout of sensors [16], as well as fast marching method and second-order difference method [17]. Dong et al. [18] proposed a location method without pre-measured wave velocity. They then optimized the method by continuously reducing the velocity interval and developed analytic and iterative cooperative localization [19]. Hesser et al. [20] applied computational intelligence to accurately identify the type of AE source based on the captured acoustic emission signals. To remove P-wave arrival time system error for each sensor, Shang et al. [21] built a Bayesian inversion framework to estimate it and proposed a high-precision virtual field optimization location method. Mostafapour et al. [22] used the theories of wavelet transform and cross-time frequency spectrum to locate AE source with frequency-varying wave velocity in plate-type structures. In addition to the artificial neural network and Bayesian methodology, scholars have applied the shuffled frog leaping algorithm to AE source localization [23–25]. These existing localization methods are partly based on the fact that the structural material of the specimen is homogeneous, i.e., the elastic wave propagates in the medium in a straight line [26–28]. However, in anisotropic plates, acoustic waves do not always propagate along a straight line. Even for isotropic plates containing empty areas or inclusions between the sound source and the AE sensor, the assumption of

* Corresponding author.
E-mail address: 0202130221@csu.edu.cn (Q. Hu).

https://doi.org/10.1016/j.ijmst.2022.01.002
2095-2686/

straight-line propagation is violated [29]. Hajzargerbashi et al. [30] argued that materials are not all homogeneous and introduced a new objective function. Experimental validation of the source localization algorithm was performed on uniformly isotropic and non-uniformly anisotropic plates. A method of AE source localization considering refraction was proposed by Zhou et al. [31] to address the problem that the existing AE source localization algorithm cannot always obtain accurate results for multi-layer cylindrical media. Baxter et al. [32] took into account the cavities in the structure, but mostly the shortest time path out of the wave is determined using a path search algorithm with the known location, size, and shape of the empty. An improved fully automated delta-T mapping technique was proposed by Al-Jumaili et al. [33]. A clustering algorithm is used to automatically identify and select highly correlated events at each grid point, while the source location is determined using the minimum difference method. Hu and Dong [34] proposed the improved A^* search algorithm to search the actual shortest time path for complex structures in irregular spaces, avoiding manual repetitive training between equidistant grid nodes and sensors. The above works considered known empty areas for AE source localization well [35]. Actually, it is extremely difficult to achieve full knowledge of the position, size, and shape of some holes hiding in the practical engineering environment [36,37].

In order to solve this problem, an AE source localization method for the target structures containing unknown holes was proposed. The method considers complex unknown empty areas encountered in the actual engineering environment. It can identify the empty areas firstly and then locate the AE sources precisely. The actual propagation path of the elastic wave in the medium is also considered, and the shortest time path of the elastic wave from the potential AE source to the sensor bypassing the empty area is tracked to make it close to the actual path to improve the location accuracy. Indoor tests were conducted to verify the proposed method using five specimens containing empty areas with different positions, shapes, and sizes. Furthermore, the effectiveness and reliability were discussed after comparing the localized results using the proposed and existing methods.

2. Methods

The AE source location method for structures containing unknown empty areas (SUEA) can be divided into two steps, including the determination of unknown empty areas and the localization of AE sources. The detailed flowchart of SUEA is shown in Fig. 1.

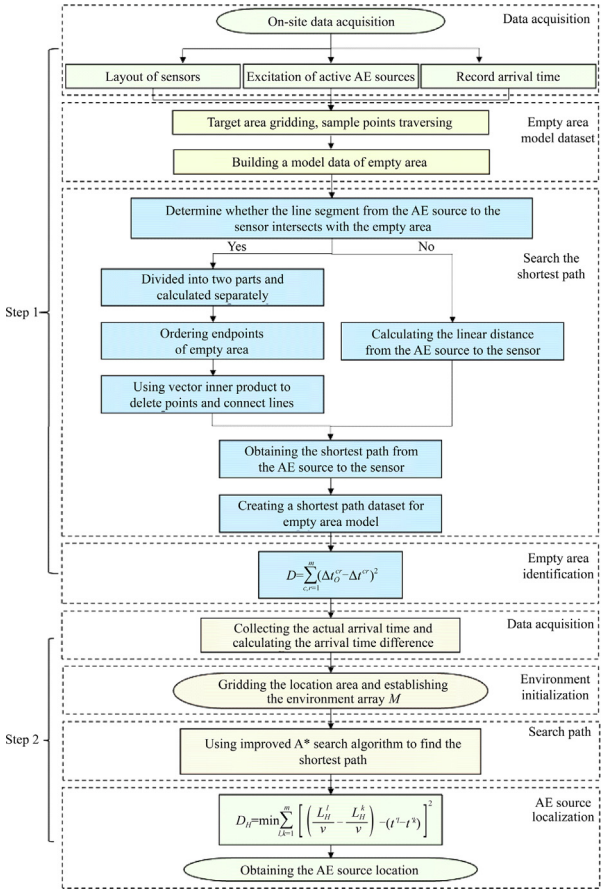

Fig. 1. Flowchart of SUEA.

2.1. Determination of unknown empty areas

2.1.1. On-site data acquisition

AE sensors are arranged at different positions in the interesting target area. The arrival time of signal from the active AE source to each AE sensor is collected on site. The position of the active AE source is actually known. The time recorded by the c-th sensor S_c is set as t^c and recorded by the r-th sensor S_r is t^r. Then the difference between the actual arrival time of the signal received by the S_c and S_r is seen in

$$\Delta t^{cr} = t^c - t^r \tag{1}$$

2.1.2. Establishing the model data of the empty area

Different empty area models would be constructed for the target area. The target area can be meshed according to a certain proportion, and grid intersections are obtained. Each grid intersection can be regarded as a sample point, and a set of sample points is obtained.

Firstly, a sample point is taken as the starting point and all available values of the empty area size are traversed. The empty area sizes take values that are integer multiples of the grid cell size and less than or equal to the size of the target area. In this study, the shapes of the empty area are divided into three categories: square, oval and horseshoe, which are the most common void shapes in the underground. Then, all the shapes of empty areas are traversed to obtain all the empty area models in the target region.

2.1.3. Calculating the shortest time path from each active AE source to each sensor in each model

(1) Determining whether the line segment from the AE source to the sensor intersects with the empty area

For convenient application, the circular shape in this study is replaced by an external cut dodecagon, and the horseshoe shape is replaced by an external cut eight-sided shape, as shown in Fig. 2. The empty area and the AE source O divide the plane into 5 parts (except the empty area, in the Fig. 2). Method description takes the square hole as an example, and the rest are similar. The directed path from the AE source O to the sensor S is defined as the vector $\overrightarrow{OS}$. The vertices of the square hole are labeled as a, b, c, and d. The vectors $\overrightarrow{Oa}, \overrightarrow{Ob}, \overrightarrow{Oc}, \overrightarrow{Od}$ are made with O as the starting point and a, b, c, d as the ending points; X_{Sa} is obtained by calculating the value of the vector outer product of $\overrightarrow{OS}(x_{OS}, y_{OS})$ and $\overrightarrow{Oa}(x_{Oa}, y_{Oa})$ (Eq. (2)).

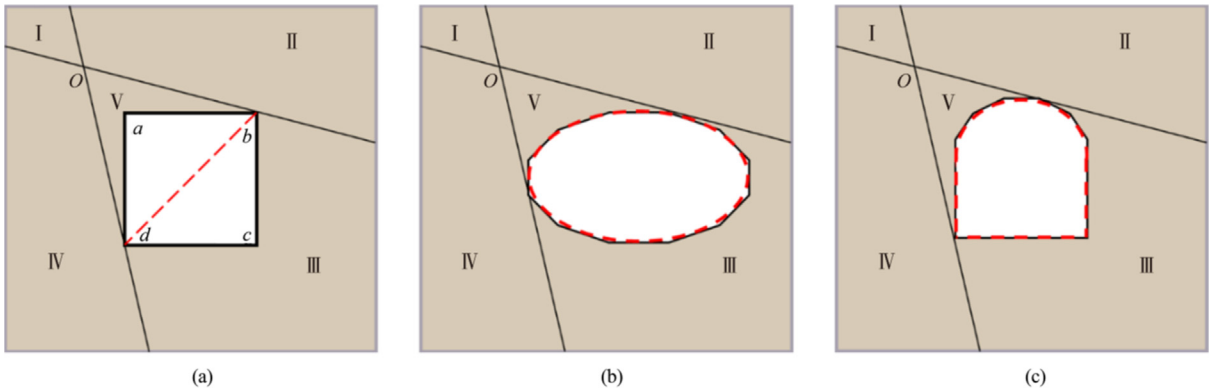

Fig. 2. A plane divided into five parts by the sensor *S* and the empty area (3 categories).

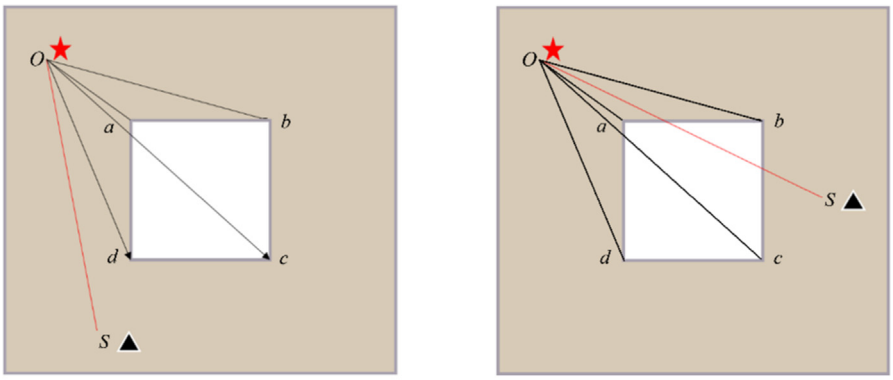

Fig. 3. Schematic diagram of AE source, sensor and empty area.

$$X_{Sa} = \overrightarrow{OS} \times \overrightarrow{Oa} = x_{OS}y_{Oa} - x_{Oa}y_{OS} \tag{2}$$

X_{Sb}, X_{Sc} and X_{Sd} are all calculated and recorded in the same way, respectively. If X_{Sa}, X_{Sb}, X_{Sc} and X_{Sd} are all non-positive or all non-negative, it means that the sensor *S* is in region II or IV.

If not, the sensor *S* would be in region I or III or V. Then, the vector inner products Y_{Sa} of the vector $\overrightarrow{OS}$ with $\overrightarrow{Oa}$ is calculated (Eq. (3)).

$$Y_{Sa} = \overrightarrow{OS} \cdot \overrightarrow{Oa} = x_{OS}x_{Oa} + y_{OS}y_{Oa} \tag{3}$$

Y_{Sb}, Y_{Sc} and Y_{Sd} are all calculated and recorded in the same way, respectively. If Y_{Sa}, Y_{Sb}, Y_{Sc} and Y_{Sd} are all negative, it means that the sensor *S* is in region I.

If not, the sensor *S* would be in region III or V. In the circumstances, the point *b* and point *d* can be determined since they correspond to the maximum and minimum values of the vector outer products $X(X_{Sa}, X_{Sb}, X_{Sc}, or\ X_{Sd})$. Then, the AE source *O* and the two points *b* and *d* form a triangle. The center of gravity method is then used to confirm whether the sensor *S* is inside the triangle. If so, it means that the sensor *S* is in the region V since the sensor *S* cannot be arranged in the empty area; if not, the sensor *S* is in region III.

If the sensor *S* is in region I or II or IV or V, the shortest time path between the AE source *O* and the sensor *S* is the length of the line segment of *OS*, as shown in Fig. 3a.

If the sensor *S* is in region III, it is the intersection problem considered in the following. The shortest time path of elastic wave between the *AE* source *O* and the sensor *S* is then calculated by bypassing the empty area, as shown in Fig. 3b. Then, the distance of the shortest time path would require further analysis, which is illustrated in steps (2) and (3) in detail.

(2) Ordering endpoints of empty area

As shown in Fig. 3b, the *OS* divides the empty area into two parts. The endpoints of two parts can be divided according to the value of the corresponding vector outer product. The endpoints in Part I have a positive value and that in Part II have the negative value, as shown in Fig. 4a. As for the endpoint with the corresponding value of 0, it can be ignored since it is on the connection line between point *O* and point *S*. Then, these two parts would be dealt with separately.

For Part I, the projection value P_{Oa} can be obtained by projecting the vectors $\overrightarrow{Oa}$ in the direction of the vector $\overrightarrow{OS}$ (Eq. (4)).

$$P_{Oa} = \frac{\overrightarrow{OS} \cdot \overrightarrow{Oa}}{\left|\overrightarrow{OS}\right|} \tag{4}$$

P_{Ob} and P_{Oc} can also be calculated and recorded in the same way in Fig. 4b. The vector projections of each part are sorted by size. According to the length of the projection, the order of the first curve segment can be obtained as *O-a-d-c-S*. Similarly, the order of another curve segment is *O-b-S*.

(3) Deleting unnecessary points

The vector angle between the vector $\overrightarrow{OS}$ and the vector $\overrightarrow{Oa}$ is calculated by Eq. (5).

$$\cos\varphi_a = \frac{\overrightarrow{OS} \cdot \overrightarrow{Oa}}{\left|\overrightarrow{OS}\right|\left|\overrightarrow{Oa}\right|} \tag{5}$$

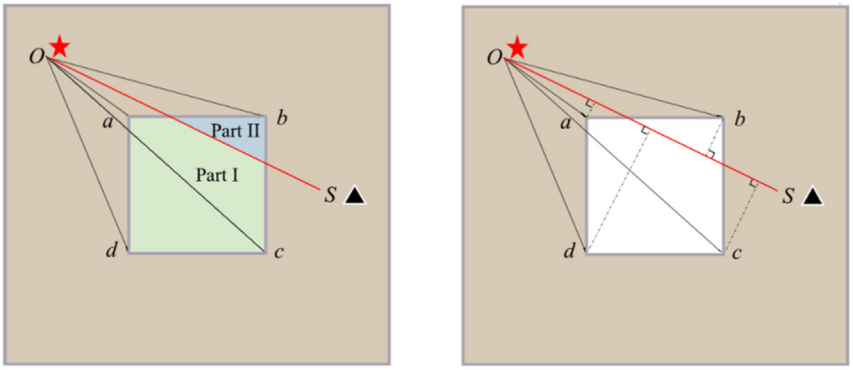

(a) $\overrightarrow{OS}$ divided the empty area into two parts (b) Projection on vector $\overrightarrow{OS}$

Fig. 4. Dividing the empty area into two parts and projecting on the vector $\overrightarrow{OS}$.

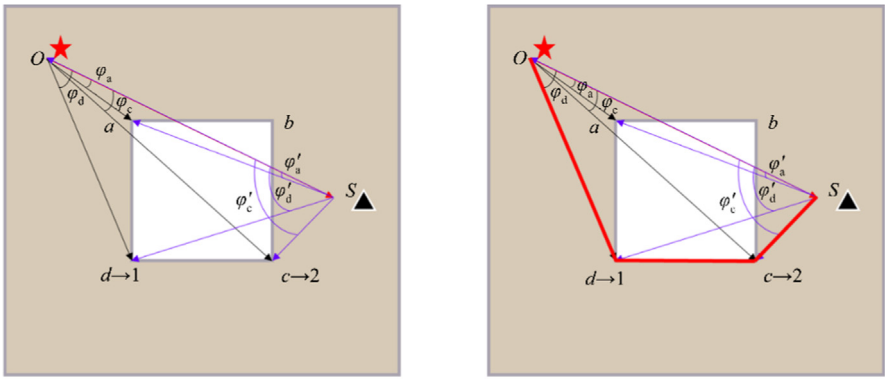

(a) Calculating the included angle (b) Finding the maximum angle and deleting the remaining points

Fig. 5. Deleting points by comparing the included angle size.

where φ_a is the angle between the vector $\overrightarrow{OS}$ and the vector $\overrightarrow{Oa}$. The same is done for the rest of the endpoints. Then, the endpoint that corresponds to the vector with the largest angle to the vector $\overrightarrow{OS}$ would be marked as endpoint 1. For example, as shown in Fig. 5a, the endpoint *d* is marked as endpoint 1. Then the vector angle of vector $\overrightarrow{SO}$ and vector $\overrightarrow{Sa}$ is calculated, and the rest of the endpoints is done in the same way. Another endpoint that corresponds to the vector with the largest angle with vector $\overrightarrow{SO}$ can be obtained and marked as endpoint 2. As shown in Fig. 5a, the endpoint *c* is then marked as 2. To ensure that the resulting path is the shortest time path for wave propagation, all endpoints between point *O* and endpoint 1 are deleted, and all endpoints between point *S* and endpoint 2 are deleted. Then, the first curve segment would become as *O*-*d*-*c*-*S*, as shown in Fig. 5b. Another curve segment would be processed in the same way, as shown in Fig. 6.

(4) Calculating the shortest path distance and building a dataset

The shortest time path is obtained by comparing the distances of two paths of the two parts. Assuming that there are *m* sensors and *n* AE sources, a single empty area model can get $m \times n$ the shortest time paths, and then the data of the shortest time path for this empty area model is established.

2.1.4. Identifying empty areas

In the empty area model data, the shortest time path between the AE source and the sensor is known. The propagation velocity of the AE source signal in the non-empty region is set as v. The value of the difference of the shortest time path between the signal excited by the AE source *O* to the AE sensor S_c and to the AE sensor S_r is ΔL_0^{cr}. Then, the difference of the theoretical travel time of the signal received by the AE sensor S_c and the AE sensor S_r is seen in Eq. (6).

$$\Delta t_0^{cr} = \Delta L_0^{cr} / v \tag{6}$$

The deviation is calculated by Eq. (7).

$$D = \sum \left(\Delta t_0^{cr} - \Delta t^{cr}\right)^2 \tag{7}$$

The smaller the value of *D*, the smaller the degree of deviation between the selected empty area model and the actual empty area. When *D* takes $D_{\min}$, the corresponding empty area model is the identified empty area.

2.2. Localization of AE sources

Based on the identification of the empty area in 2.1, AE sources are located in the target area.

2.2.1. Data acquisition

Receiving the acoustic signal (P-wave signal) generated by the unknown actual AE source through the AE sensor, the actual time is recorded as t'^k at which the *k*-th AE sensor S_k receives the acoustic signal.

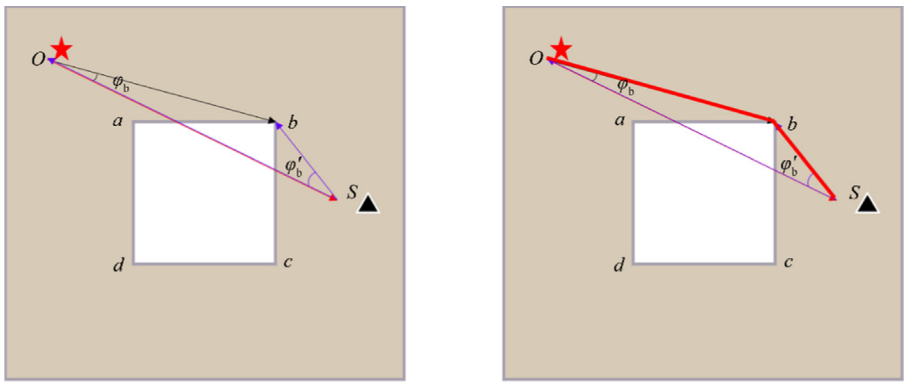

Fig. 6. The shortest path on the other side.

2.2.2. Calculation of theoretical values

The target area is gridded at a certain scale to get n grid intersections. Each grid intersection is treated as a node, and a set of n nodes is obtained. An array M is created, and the elements in M correspond to the nodes one by one. If a node falls in a solid region in the target area, its corresponding element in the M matrix is set to 0, representing a passable position for that node. If a node falls in an empty area in the target region, its corresponding element in the M matrix is set to 1, which means that the node position is not passable.

All the nodes in the set are traversed, and each node H is regarded as the potential AE source location. And the following processing are performed:

The improved A^* shortest path search algorithm is used to track the shortest time path of signal propagation between H and the k-th AE sensor S_k, denoted as L_H^k; If H is in the empty area, then $L_H^k = \infty$; Compared with the A^* search algorithm, the improved A^* search algorithm adapts grid points instead of center points to search the paths which are more in line with the actual boundary of the empty region. Besides, the improved A^* search algorithm can search more accurate paths by using more connection nodes [34].

2.2.3. Locating calculation

D_H is introduced to describe the degree of the deviation of each node H from the actual AE source location is estimated. The node with the smallest deviation from the actual AE source position among all nodes is determined, and the coordinates of this node are used as the positioning coordinates of the actual AE source. D_H is calculated as shown in Eq. (8).

$$D_H = \min \sum \left[\left(\frac{L_H^l}{v} - \frac{L_H^k}{v} \right) - (t'^l - t'^k) \right]^2 \tag{8}$$

A smaller value of D_H indicates that the deviation of node H from the actual AE source location is the smaller, and thus the node corresponding to the smallest D_H is regarded as the position of the actual AE source.

3. Experiments

To verify the practical feasibility of this method for complex structural empty area identification and localization, AE tests were carried out on five square rock slabs containing empty areas of different shapes and sizes. The AE monitoring equipment that used was the AMSY-6 multi-channel device (composed of parallel measurement channels) from Vallen, Germany. The system has 32 channels for AE signal acquisition, with a sampling frequency of 10 MHz and a preamplifier gain of 34 dB. It can be used to identify, measure and locate the AE sources of materials. It records information on the temporal and spatial changes of micro-level damage of the test object in the case of rupture, corrosion, leakage, partial discharge, friction, and wear, as well as impact. The system is equipped with the dual channel AE signal processor ASIP-2, which has a resolution of up to 40 MHz sampling rate at an 18-bit dynamic range and a high sensitivity. The acquisition of AE signals is carried out simultaneously during the test, and the acquisition and analysis of AE characteristic parameters and waveforms are carried out. The type of AE sensor adopted is VS45-H. The VS45-H is a passive piezoelectric AE sensor with a wide frequency response. Its frequency response is characterized by a peak at 280 kHz and can be used in the frequency range from 20 to 450 kHz. It is a broad band response AE sensor covering the range of low frequency and standard frequency. The main chassis adopts military grade VME bus structure with multiple transmission modes. The transmission speed can reach 5 Gbps, which can better meet the measurement and analysis requirements of this test.

The common rock slabs with less anisotropy were used in the test. Five square rock slabs with dimensions of 60 cm × 60 cm and thickness of about 1 cm were used. On the rock slab, 20 cm × 20 cm square holes, 20 cm × 40 cm rectangular holes, R=10 cm circular holes, a=20 cm, b=10 cm oval holes and horseshoe-shaped holes consisting of 20 cm square sides and 10 cm radius semicircle were machined and cut respectively. The parallelism, flatness, and perpendicularity of the rock sample were in accordance with the test protocol. The specimen, AE sensor, preamplifier, AE detector and computer were connected in an orderly manner. An appropriate amount of Vaseline was applied between the sensor and the specimen to obtain better acoustic coupling, and a layer of acoustic bubble paper was placed underneath the specimen to reduce the effect of noise. Fig. 7 shows the schematic diagram of the test setup.

In order to identify and locate the empty area, a total of 28 sensors were arranged around each specimen in this experiment. Their relative positions are shown in Fig. 7. The coordinate system is also shown in Fig. 7 and the coordinates of the sensor positions are shown in Table 1.

Lead break tests were conducted next to each sensor before starting the experiment. It was determined that the amplitude of the lead-breaking signal received by each sensor from the adjacent source was above 95 dB to ensure the coupling quality of the sensor and the specimen. Considering reducing the influence of environmental noise and improving the reliability of signal acquisition,

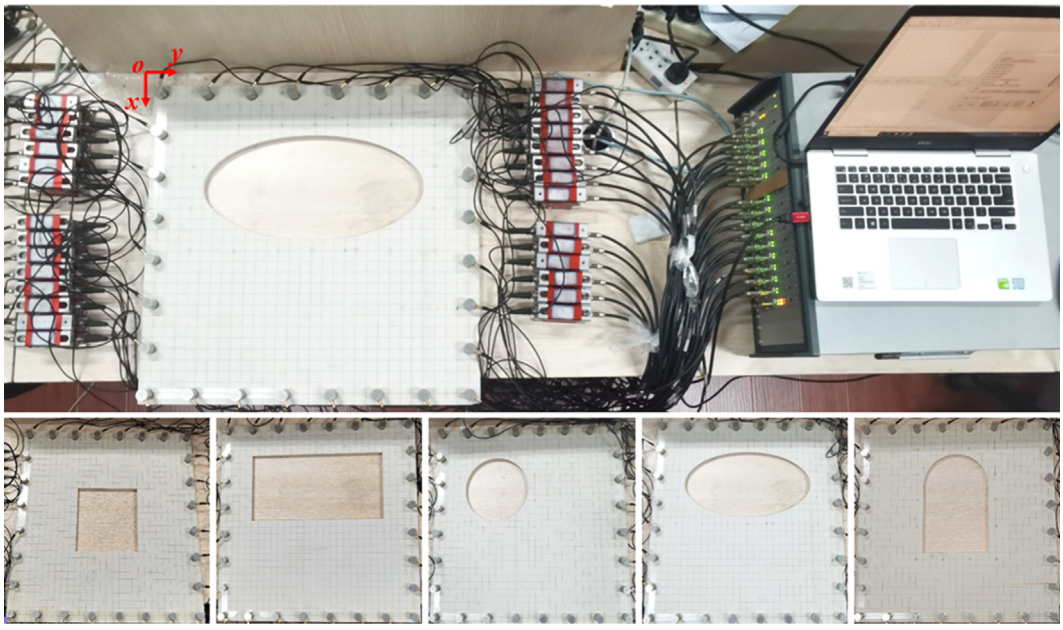

Fig. 7. Experimental setup diagram.

Table 1
Sensors position coordinates.

No.	*x* (cm)	*y* (cm)	No.	*x* (cm)	*y* (cm)
1	2	2	15	58	58
2	2	10	16	58	50
3	2	18	17	58	42
4	2	26	18	58	34
5	2	34	19	58	26
6	2	42	20	58	18
7	2	50	21	58	10
8	2	58	22	58	2
9	10	58	23	50	2
10	18	58	24	42	2
11	26	58	25	34	2
12	34	58	26	26	2
13	42	58	27	18	2
14	50	58	28	10	2

the threshold was set at 35 dB according to the monitoring results of environmental background noise.

The experimental procedure was divided into two parts: empty area identification and AE source localization.

(1) Empty area identification
During the experiment, the pulse signal from the sensor was used as the AE source. The pulse emission time interval was 1 s. There were 28 channels, and each channel emitted 4 pulses. The AE acquisition system recorded the initial arrival time of each sensor.

(2) AE source localization
The points next to the empty area were selected for the lead break. This is because the edge stress of the empty area is high and it is easy to crack, which is used to simulate the fracture signal. In order to avoid the adverse effects of human errors on the experiment during lead breaking, a diameter of 0.5 mm and hardness of HB pencil core with a special pencil (which can ensure a 30° angle between the core and the surface of the rock slab) was used.

4. Results and discussion

In order to explore the problem of AE source localization in the target area containing unknown empty area, a newly AE source localization method is proposed and the validity of the method is

Table 2
Location results of Specimen 1.

No.	Actual lead break point (cm)		SUEA location result (cm)		SUEA location error (cm)	TD location result (cm)		TD location error (cm)
1	18	18	17	17	1.4	19.3	18.4	1.3
2	18	26	17	26	1.0	5.5	28.8	12.8
3	18	34	17	34	1.0	12.4	35.9	6.0
4	18	42	18	42	0	19.4	41.2	1.6
5	26	42	25	42	1.0	24.0	45.7	4.2
6	34	42	34	42	0	34.7	44.7	2.8
7	42	42	43	43	1.4	40.3	39.5	3.0
8	42	34	44	35	2.2	44.0	35.2	2.3
9	42	26	44	24	2.8	45.0	23.9	3.7
10	42	18	42	18	0	41.9	18.9	0.9
11	34	18	34	17	1.0	34.9	15.5	2.6
12	26	18	25	17	1.4	25.4	15.6	2.5
Average Error					1.1			3.6

Table 3
Location results of Specimen 2.

No.	Actual lead break point (cm)		SUEA location result (cm)		SUEA location error (cm)	TD location results (cm)		TD location errors (cm)
1	8	8	8	8	0	10.1	8.6	2.2
2	8	16	7	16	1.0	10.8	18.2	3.6
3	8	24	7	24	1.0	0	22.0	8.2
4	8	30	8	30	0	0	32.2	8.3
5	8	36	8	36	0	0	39.0	8.6
6	8	44	2	43	6.1	3.2	43.7	4.8
7	8	52	8	52	0	10.3	51.7	2.3
8	16	52	15	54	2.2	14.3	60.0	8.2
9	24	52	24	54	2.0	28.4	60.0	9.1
10	32	52	32	54	2.0	34.2	47.7	4.8
11	32	44	32	45	1.0	39.0	42.7	7.1
12	32	36	32	37	1.0	40.7	38.1	8.9
13	32	30	32	30	0	44.7	31.8	12.8
14	32	24	32	25	1.0	40.9	23.2	9.0
15	32	16	32	14	2.0	39.1	14.7	7.2
16	32	8	32	7	1.0	35.5	13.5	6.5
17	24	8	23	6	2.2	28.0	9.5	4.2
18	16	8	15	6	2.2	14.5	0	8.1
Average Error					1.4			6.9

Table 4
Location results of Specimen 3.

No.	Actual lead break point (cm)		SUEA location result (cm)		SUEA location error (cm)	TD location result (cm)		TD location error (cm)
1	8	8	7	8	1.0	9.2	9.6	2.0
2	8	16	8	15	1.0	8.3	16.2	0.3
3	8	24	8	24	0	8.4	25.9	1.9
4	8	32	9	31	1.4	7.7	33.4	1.4
5	16	32	15	33	1.4	15.2	34.7	2.8
6	24	32	23	33	1.4	25.0	33.5	1.8
7	32	32	31	32	1.0	32.4	32.2	0.5
8	32	24	32	24	0	33.7	25.1	2.0
9	32	16	32	16	0	33.6	16.6	1.7
10	32	8	32	8	0	33.0	7.7	1.0
11	24	8	24	8	0	25.6	8.3	1.6
12	16	8	16	9	1.0	16.8	8.5	1.0
Average Error					0.7			1.5

Table 5
Location results of Specimen 4.

No.	Actual lead break point (cm)		SUEA location result (cm)		SUEA location error (cm)	TD location result (cm)		TD location error (cm)
1	8	8	8	8	0	8.8	8.8	1.1
2	8	16	7	15	0	11.0	17.2	3.2
3	8	24	6	23	3.2	0	21.2	8.5
4	8	30	5	29	3.0	0	31.1	8.1
5	8	36	8	35	0	10.4	36.1	2.4
6	8	44	8	43	0	11.2	43.1	3.3
7	8	52	8	52	0	10.4	50.3	3.0
8	16	52	16	51	0	17.3	50.6	1.9
9	24	52	24	52	0	26.2	50.0	3.0
10	32	52	32	52	1.0	33.1	48.9	3.3
11	32	44	32	44	0	36.3	43.2	4.3
12	32	36	31	36	1.0	39.8	39.0	8.4
13	32	30	32	30	1.0	38.4	30.4	6.4
14	32	24	31	24	1.0	37.9	21.4	6.4
15	32	16	32	16	1.0	36.8	15.0	4.9
16	32	8	32	9	0	34.0	12.0	4.5
17	24	8	23	9	1.4	25.9	9.2	2.3
18	16	8	16	8	0	16.6	8.9	1.0
Average Error					0.7			4.2

verified by experiments. For each lead break point, SUEA and TD [38] these two location methods were used for locating and error analysis, and the location results are shown in Tables 2-6. In order to display the location results more visually, the location results of the five specimens are plotted as shown in Fig. 8. As can be seen from the results, the new location method got satisfactory results on all five specimens. The location errors of SUEA are less than or equal to 2.0 cm (less than the diameter of the sensor) for almost all of source points in five tests, while that of TD for most source points are larger than 2.0 cm.

According to the new AE source location method, the largest location error is 2.8 cm and the smallest error is 0 cm in the 12 lead breaking points of Specimen 1. Among the 18 lead breaking points of Specimen 2, the largest location error is 6.1 cm, and the smallest error is 0 cm. The average location error of Specimen 2 is 1.4 cm, which is the largest average location error among five specimens. Among the 12 lead break points of Specimen 3, the largest location error is 1.4 cm and the smallest error is 0 cm. Specimen 4 has the largest location error of 3.2 cm and the smallest error of 0 cm among the 18 lead break points. At last Specimen 5 has the largest location error of 1.4 cm and the smallest error of 0 cm among the 14 lead breaks points.

As a control, the TD location method was chosen to locate the lead break points. The reason for choosing TD is that this method can get a high-accuracy location result and does not require a pre-measured velocity [36]. Therefore, the location results of TD was chosen for comparison.

TD location results show that in Specimen 1, the largest location error is 12.8 cm and the smallest error is 0.9 cm. In Specimen 2, the largest location error is 12.8 cm and the smallest error is 2.2 cm, which is the largest average location error among the five specimens. In Specimen 3, the largest location error was 2.8 cm and the smallest error was 0.3 cm, and Specimen 3 was also the one with the smallest average location error among the five specimens.

Table 6
Location results of Specimen 5.

No.	Actual lead break point (cm)		SUEA location result (cm)		SUEA location error (cm)	TD location result (cm)		TD location error (cm)
1	8	18	8	18	0	11.3	18.7	3.3
2	8	26	8	26	0	9.5	25.9	1.5
3	8	34	8	34	0	10.1	34.9	2.2
4	8	42	9	41	1.4	11.9	40.6	4.1
5	16	42	17	41	1.4	17.6	42.3	1.7
6	24	42	24	41	1.0	22.4	46.7	5.0
7	32	42	31	41	1.4	33.6	44.4	2.8
8	42	42	42	42	0	40.4	40	2.5
9	42	34	43	35	1.4	43.5	35.9	2.5
10	42	26	43	25	1.4	44.7	24.4	3.2
11	42	18	42	18	0	40.6	19.4	2.0
12	32	18	32	18	0	33.1	15.7	2.5
13	24	18	23	17	1.4	22.5	12.9	5.3
14	16	18	16	18	0	17.0	16.5	1.8
Average Error					0.7			2.9

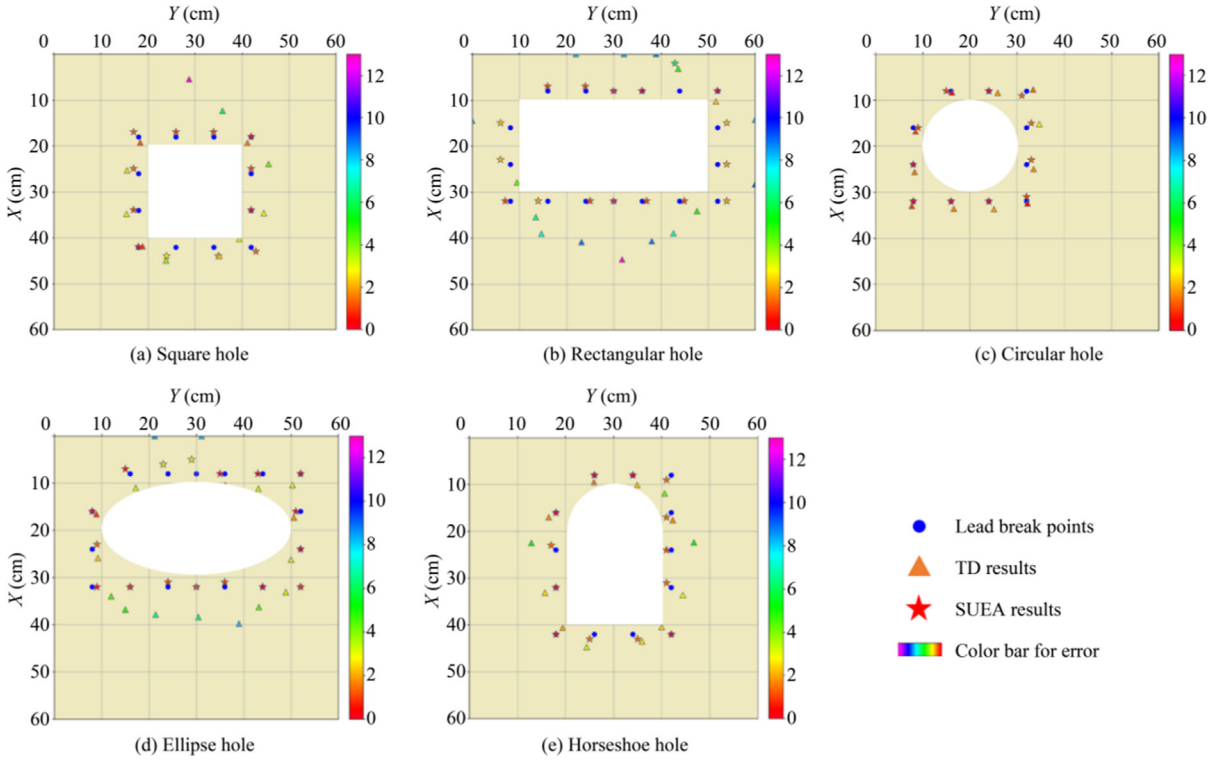

Fig. 8. SUEA and TD location results.

In Specimen 4, the largest location error was 8.5 cm and the smallest error was 1.0 cm. In Specimen 5, the largest location error was 5.3 cm and the smallest error was 1.5 cm.

For further analysis, the average location errors of SUEA for specimens 1–5 were calculated and the corresponding values are 1.1, 1.4, 0.7, 0.7, and 0.7 cm. The average location errors of TD location method are 3.6, 6.9, 1.5, 4.2, and 2.9 cm. Because the traditional method cannot bypass the empty area, the location result has a large deviation from the actual situation. Compared with the TD location method, the new method showed a significant reduction in the average location error on the five specimens. The average location error of the new method is only 22% of that of the traditional location method.

This indicates that the accuracy of the new location method has been improved significantly. This is because the new method takes into account that the presence of potential unknown empty areas, which can significantly affect the location accuracy of the conventional location method. The new method could identify the potential unknown empty area and then locate the AE source, which can effectively solve the problem of locating the AE source in complex areas containing unknown empty areas. The results of the empty area identification are shown in Table 7 and Fig. 9, which are in line with the actual situation.

Table 7
Empty area identification results.

No.	Actual empty area location (cm)	Identification result (cm)
1	20,20,20,20	18,18,26,24
2	10,10,20,40	10,6,22,48
3	10,10,20,20	6,10,26,22
4	10,10,20,40	10,8,22,44
5	10,20,20,20	8,18,24,22

Notes: The first two numbers represent the coordinates of the endpoints of the empty area near the origin of the coordinates (circles and ellipses are based on their external tangent squares); and the last two numbers represent the two side lengths of the empty area in the *x* and *y* directions.

In the actual mining, cavern, tunnel and other environments, the strata will encounter complex empty areas such as roadways and quarries. Using AE technology to monitor and locate the areas with cavities is a hot issue at this stage. There are two main types of problems with the currently existing AE localization methods: one is that the empty area is not taken into account, and the travel path of the wave between the source and the AE sensor is assumed to be a straight-line path; the other is that localization can only be performed on the basis of a known empty area. As we all know, elastic waves propagate much faster in solids than in air. Therefore, waves that bypass the empty area will reach the sensor location faster and be recorded by the sensor in the structure with complex empty areas. In this case, for the first type of methods, the assumption that the travel path of the wave between the AE source and the AE sensor is a straight line will no longer meet the actual situation. Besides, in the actual engineering environment, it is impossible to know all the empty positions in each area to be located. So the application of the second type of methods is very limited. The newly proposed localization method can realize the precise localization of AE sources under the premise that the location of the empty in the target area is unknown.

This method takes into account the fact that the empty location will be encountered in the actual engineering environment where it is difficult to identify, making the accuracy of AE source localization in complex environments much higher and improving the application range. However, this research also has the following limitations.

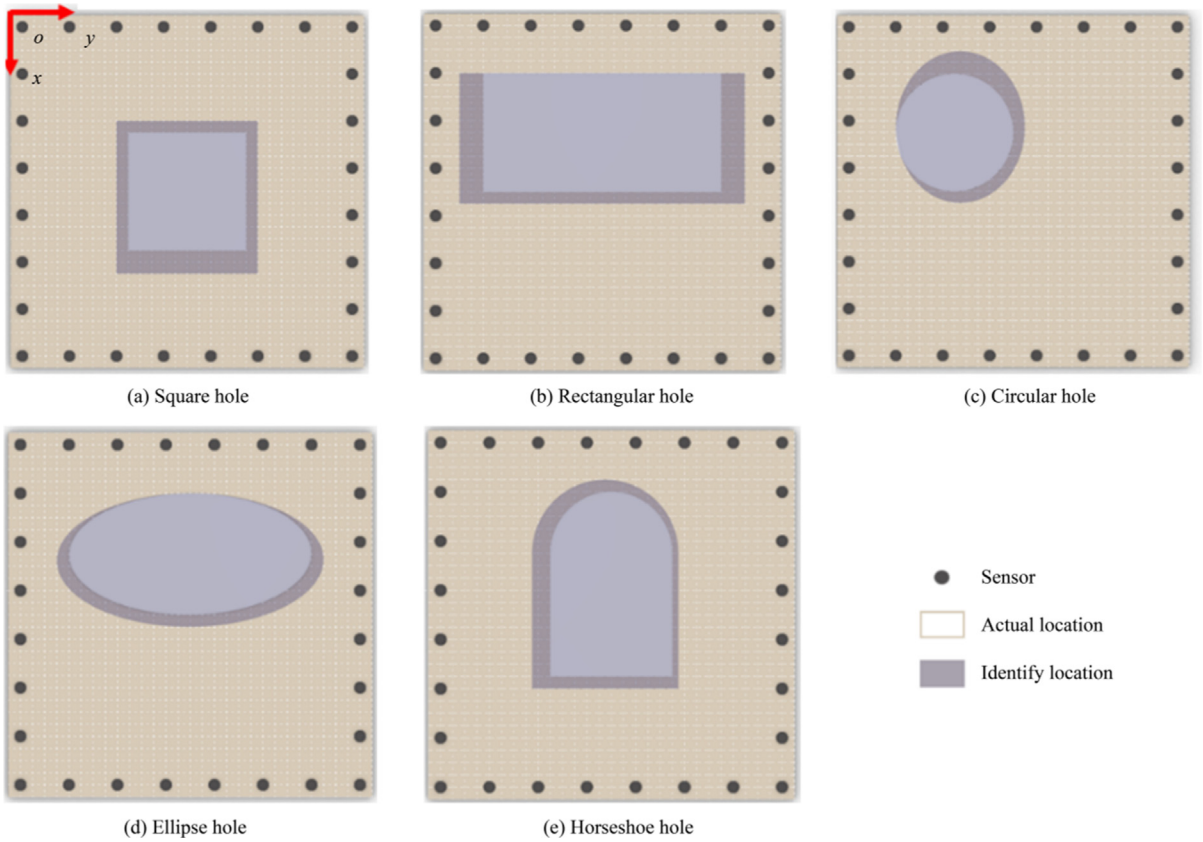

Fig. 9. Five test pieces empty area identification results.

(1) The sensor size is too large, which affects the wave velocity. The pulse signal emitted by any sensor is used as the AE source, and the remaining 27 sensors receive the AE signal. The shortest time paths of wave propagation from the AE source to 27 sensors are calculated respectively. Combined with the arrival times collected by the AE acquisition system, it can be seen that the wave velocity is relatively small at a distance far from the AE source and relatively large at a distance close to the AE source. The reason for this may be that when a sensor is excited and receives a pulse signal, it transmits and receives the signal on a plane rather than a single central point. Therefore, when a sensor emits a pulse signal, the area of the receiving sensor that is the closest to the emitting sensor is the first to receive the signal. So the shortest time path of the actual elastic wave is the shorter than the distance from the point of pulse emission to the center of the sensor. In the path search dataset with empty areas, the theoretical path is larger than the actual path. The wave velocity $v = s/t$, when s is larger, the incremental Δs caused by the AE signal being a surface source instead of a point source has a smaller or negligible effect on the wave velocity; when s is smaller, the effect of Δs on the wave velocity is larger.

(2) The ray density is too small. Using the pulse signal excited by the sensor as the active AE source, the distance between two adjacent sensors is 8 cm by dividing the grid. The sensors are not closely arranged, resulting in a small ray density. This causes large errors when identifying small empty areas. If the number of sensors is increased or the number of AE sources is increased (e.g., more lead break points are used as active AE sources), the discrimination effect will be better, and thus the location accuracy will be higher.

(3) Traversing all shapes is obviously not feasible due to computational and time costs. In the next step, an attempt is made to construct arbitrarily complex shapes using basic shapes such as squares and ellipses to realize the reuse of the data. For example, the horseshoe shape can be decomposed into a square and a half ellipse. In addition, this study carries out experimental research in a two-dimensional plane of 60 cm × 60 cm, and will be expanded to three-dimensional space in the future to make this study more scientifically valuable and practically meaningful.

5. Conclusions

The empty areas widely exist in practical engineering and it is difficult to obtain the information of holes that hide in the structure, which have a great impact on the location accuracy of AE sources. SUEA is proposed to reduce the impact in this paper. In order to verify the accuracy of the method proposed in this paper, five specimens with different shapes, sizes, and positions of empty areas are selected. The following conclusions were obtained:

(1) The proposed method SUEA not only overcomes the defect that existing methods assume that the path between the sensor and the AE source is a straight path, but also solves the influence of unknown empty area on location accuracy.

(2) The lead break experiment was carried out and results show the average location accuracy of the SUEA increased by 78% compared to the results of the existing method TD.

This means that the newly proposed localization method can achieve more effective and accurate localization of AE sources in areas containing unknown empty areas. It not only provides the theoretical basis and technical support for the detection of abnormal regions and localization of AE sources in complex structures, but also benefits for prediction and control of engineering disasters.

Acknowledgements

We are grateful for the financial support from the National Science Foundation for Excellent Young Scholars of China (51822407), the Natural Science Foundation of China (51774327), the Special Fund for Basic Scientific Research Operations in Universities (2282020cxqd055), and the Fundamental Research Funds for the Central Universities of Central South University (2021zzts0875).

References

[1] Shanyavskiy A, Banov M. Acoustic emission methods for lifetime estimations in aircraft structures. Theor Appl Fract Mech 2020;109:102719.
[2] Meserkhani A, Jafari SM, Rahi A. Experimental comparison of acoustic emission sensors in the detection of outer race defect of angular contact ball bearings by artificial neural network. Measurement 2021;168:108198.
[3] Ran H, Guo Y, Feng G, Qi T, Du X. Creep properties and resistivity-ultrasonic-AE responses of cemented gangue backfill column under high-stress area. Int J Min Sci Techno 2021;31(3):401–12.
[4] Wang S, Liu C, Shao Z, Ma G, He C. Experimental study on damage evolution characteristics of segment structure of shield tunnel with cracks based on acoustic emission information. Eng Fail Anal 2020;118:104899.
[5] De Santis S, Tomor AK. Laboratory and field studies on the use of acoustic emission for masonry bridges. NDT and E Int 2013;55:64–74.
[6] Zhang X, Wang K, Wang Y, Shen Yi, Hu H. Rail crack detection using acoustic emission technique by joint optimization noise clustering and time window feature detection. Appl Acoust 2020;160:107141.
[7] Xue DJ, Zhang ZP, Chen C, Zhou J, Lu Lan, Sun XT, Liu YT. Spatial correlation-based characterization of acoustic emission signal-cloud in a granite sample by a cube clustering approach. Int J Min Sci Technol 2021;31(4):535–51.
[8] Giridhar D, Vijayaraghavan L, Krishnamurthy R. Acoustic emission response of sintered alumina zirconia composite during grooving process. NDT E Int 2012;46:55–62.
[9] Dong LJ, Chen YC, Sun DY, Zhang YH. Implications for rock instability precursors and principal stress direction from rock acoustic experiments. Int J Min Sci Techno 2021;31(5):789–98.
[10] Becker D, Cailleau B, Dahm T, Shapiro S, Kaiser D. Stress triggering and stress memory observed from acoustic emission records in a salt mine. Geophys J Int 2010;182(2):933–48.
[11] Davydova DG, Kuz'min AN, Rizvanov RG, Aksel'rod EG. Identification of acoustic-emission sources during testing of technological equipment with a high noise level. Russ J Nondestr Test 2015;51(5):292–302.
[12] Wang JX, Tang SB, Heap MJ, Tang CA, Tang LX. An auto-detection network to provide an automated real-time early warning of rock engineering hazards using microseismic monitoring. Int J Rock Mech Min Sci 2021;140:104685.
[13] Zhu W, Yao N, Yan J. Exploring the determinants of disaster coverage: Evidence from coal mine disasters coverage in China. Int J Disaster Risk Reduct 2018;31:856–61.
[14] Jiao J, Wu B, He C. Acoustic emission source location methods using mode and frequency analysis. Struct Control Health Monitor 2008;15(4):642–51.
[15] Park B, Sohn H, Olson SE, DeSimio MP, Brown KS, Derriso MM. Impact localization in complex structures using laser-based time reversal. Struct Health Monit 2012;11(5):577–88.
[16] Zhang ZN, Tian J. A New Acoustic Emission Source Location Method Based on the Linear Layout of Sensors. Adv Mater Res 2011;267:561–4.
[17] Jiang R, Dai F, Liu Y, Li A. Fast Marching Method for Microseismic Source Location in Cavern-Containing Rockmass. Perform Anal Eng Appl Eng 2021;7(7):1023–34.
[18] Dong LJ, Li XB. Three-dimensional analytical solution of acoustic emission or microseismic source location under cube monitoring network. Trans Nonferrous Metals Soc China 2012;22(12):3087–94.
[19] Dong LJ, Zou W, Li XB, Shu WW, Wang ZW. Collaborative localization method using analytical and iterative solutions for microseismic/acoustic emission sources in the rockmass structure for underground mining. Eng Fract Mech 2019;210:95–112.
[20] Hesser DF, Mostafavi S, Kocur GK, Markert B. Identification of acoustic emission sources for structural health monitoring applications based on convolutional neural networks and deep transfer learning. Neurocomputing 2021;453:1–12.
[21] Shang XY, Wang Y, Miao RX. Acoustic emission source location from P-wave arrival time corrected data and virtual field optimization method. Mech Syst Sig Process 2022;163:108129.

[22] Mostafapour A, Davoodi S, Ghareaghaji M. Acoustic emission source location in plates using wavelet analysis and cross time frequency spectrum. Ultrasonics 2014;54(8):2055–62.
[23] Cheng XM, Zhang XD, Zhao L, Deng AD, Bao YQ, Liu Y, Jiang YL. The application of Shuffled Frog Leaping Algorithm to Wavelet Neural Networks for acoustic emission source location. Comptes Rendus Mécanique 2014;342(4):229–33.
[24] Jones MR, Rogers TJ, Worden K, Cross EJ. A Bayesian methodology for localising acoustic emission sources in complex structures. Mech Syst Sig Process 2022;163:108143.
[25] Xu NW, Dai F, Zhou Z, Jiang P, Zhao T. Microseismicity and its time–frequency characteristics of the left bank slope at the Jinping first-stage hydropower station during reservoir impoundment. Environ Earth Sci 2016;75:608.
[26] Kundu T. Acoustic source localization. Ultrasonics 2014;54(1):25–38.
[27] Sedlak P, Hirose Y, Khan SA, Enoki M, Sikula J. New automatic localization technique of acoustic emission signals in thin metal plates. Ultrasonics 2009;49(2):254–62.
[28] Jiao JP, He CF, Wu B, Fei RY, Wang XY. Application of wavelet transform on modal acoustic emission source location in thin plates with one sensor. Int J Press Vessels Pip 2004;81(5):427–31.
[29] Kundu T, Yang X, Nakatani H, Takeda N. A two-step hybrid technique for accurately localizing acoustic source in anisotropic structures without knowing their material properties. Ultrasonics 2015;56:271–8.
[30] Hajzargerbashi T, Kundu T, Bland S. An improved algorithm for detecting point of impact in anisotropic inhomogeneous plates. Ultrasonics 2011;51(3):317–24.
[31] Zhou ZL, Zhou J, Cai X, Rui YC, Chen LJ, Wang HQ. Acoustic emission source location considering refraction in layered media with cylindrical surface. Trans Nonferrous Metals Soc China 2020;30(3):789–99.
[32] Baxter MG, Pullin R, Holford KM, Evans SL. Delta T source location for acoustic emission. Mech Syst Sig Process 2007;21(3):1512–20.
[33] Al-Jumaili SK, Pearson MR, Holford KM, Eaton MJ, Pullin R. Acoustic emission source location in complex structures using full automatic delta T mapping technique. Mech Syst Sig Process 2016;72-73:513–24.
[34] Hu QC, Dong LJ. Acoustic Emission Source Location and Experimental Verification for Two-Dimensional Irregular Complex Structure. IEEE Sens J 2020;20(5):2679–91.
[35] Dong LJ, Hu QC, Tong XJ, Liu YF. Velocity-Free MS/AE Source Location Method for Three-Dimensional Hole-Containing Structures. Engineering 2020;6(7):827–34.
[36] Dong LJ, Tong XJ, Ma J. Quantitative Investigation of Tomographic Effects in Abnormal Regions of Complex Structures. Engineering 2021;7(7):1011–22.
[37] Dong LJ, Tong XJ, Hu QC, Tao Q. Empty region identification method and experimental verification for the two-dimensional complex structure. Int J Rock Mech Min Sci 2021;147:104885.
[38] Dong LJ, Li XB, Tang LZ, Gong FQ. Mathematical Functions and Parameters for Microsesmic Source Location without Pre-measuring Speed. Chin J Rock Mech Eng 2011;30(10):2057–67.